

Structural metastability and Fermi surface Topology of SrAl_2Si_2

Stamatios Strikos,^{*,†} Bobby Joseph,[‡] Frederico G. Alabarse,[‡] George Valadares,[¶]
Deyse G. Costa,[§] Rodrigo B. Capaz,[†] and Mohammed ElMassalami^{*,†}

[†]*Instituto de Física, Universidade Federal do Rio de Janeiro, CxP 68528, 21945-972 Rio de Janeiro, Brazil*

[‡]*Elettra-Sincrotrone Trieste, S.S. 14 – km 163,5, Area Science Park 34149 Basovizza, Trieste, Italy*

[¶]*Universidade Federal do Acre, Rodovia BR 364, Km 04, Distrito Industrial, Rio Branco, AC, 69920-900, Brazil*

[§]*Departamento de Química, Universidade Federal da Viçosa, Viçosa, Caixa Postal 216, Brazil*

E-mail: stamostrik@pos.if.ufrj.br; massalam@if.ufrj.br

Abstract

SrAl₂Si₂ crystallizes into either a semimetallic, CaAl₂Si₂-type, α phase or a superconducting, BaZn₂P₂-type, β phase. We explore possible $\alpha \xrightarrow{P_c, T_c} \beta$ transformations by employing pressure- and temperature-dependent free-energy calculations, vibrational spectra calculations, and room-temperature synchrotron X-ray powder diffraction (XRPD) measurements up to 14 GPa using diamond anvil cell. Our theoretical and empirical analyses together with all baric and thermal reported events on both phases allow us to construct a preliminary P - T diagram of transformations. Our calculations show a relatively low critical pressure for the α to β transition (4.9 GPa at 0 K, 5.0 GPa at 300 K and 5.3 GPa at 900 K); nevertheless, our nonequilibrium analysis indicates that the low-pressure-low-temperature α phase is separated from metastable β phase by a relatively high activation barrier. This analysis is supported by our XRPD data at ambient temperature and $P \leq 14$ GPa which shows an absence of β phase even after a compression involving three times the critical pressure. Finally, we briefly consider the change in Fermi surface topology when atomic rearrangement takes place via either transformations among SrAl₂Si₂-dimorphs or total chemical substitution of Ca by Sr in isomorphous α CaAl₂Si₂; empirically, manifestation of such topology modification is evident when comparing the evolution of (magneto-)transport properties of members of SrAl₂Si₂-dimorphs and α isomorphs.

1 Introduction

Generally, a phase diagram of a polymorph exhibits a cascade of transformations among distinct phases.¹⁻⁴ Based on consideration of energy landscape, some metastable phases are separated from the stable ones by a steep energy barrier such that a transformation among them can only be effected by energy-yielding control parameters such as pressure and temperature. On the other hand, consideration of kinetics enables one to identify non-equilibrium features such as (ir)reversibility of the transformation and (meta)stability of the induced phases. Various equilibrium and non-equilibrium techniques with adequate frequency and spacial resolution can be used to probe both the transformations and the induced phases. The obtained results are often compiled in, e.g. P - T diagram of transformations; usually these diagrams include adequate specification of characteristics such as (meta)stability, (ir)reversibility, and thermodynamic parameters (e.g. order and rate of transformation as well as the involved energetics).

As an illustration, let us recall the transformations and phases encountered in the P - T phase diagram of carbon wherein the two allotropes (namely metastable diamond and stable graphite) are separated by a very high

activation barrier.^{5,6} In contrast to these extreme conditions, there are various other transformations and induced phases which can be carried out under modest laboratory conditions. Below, on employing experimental techniques (pressure-dependent structural analysis) and theoretical (equilibrium free-energy and vibrational spectra) analysis, we are able to construct and analyze a P - T diagram of transformation of another example of a polymorphic system, namely the semimetallic layered SrAl₂Si₂. As will be shown, much insight is gained on analyzing the (ir)reversibility of its structural transformations and the (meta)stability of its induced crystalline phases.

SrAl₂Si₂ crystallizes into two layered phases (see Fig. 1). The first, so-called α phase, exhibits a stable trigonal ($P\bar{3}m1$) structure wherein slabs of three-edges-sharing tetrahedrally-coordinated AlSi₄ are intercalated, along the c -axis, with Sr planes.⁷⁻⁹ The related electronic structure exhibits a series of hole and electron pockets contributing to a total density of states (DOS at E_F , $N_t(E_F)$) which is relatively lower than the one observed in isomorphous α CaAl₂Si₂.^{8,9} The observed electrical transport properties were reported to be non-superconducting semimetallic with dominant contribution from electron charge carriers.⁷⁻⁹

The second, so called β phase, is metastable at low pressures and exhibits BaZn₂P₂-type ($I4/mmm$) layered structure wherein slabs of four-edges-sharing AlSi₄ are intercalated, along the c -axis, with Sr planes¹⁰ (see also Fig. 1). Its electronic structure is metallic, with predominantly electronic charge carriers, and exhibits a relatively higher $N_t(E_F)$; this is assumed to be the driving ingredient behind the surge of superconductivity below $T_c \approx 2.6$ K.⁹

The β phase can be stabilized by quenching of the high-pressure and high-temperature (HPHT) phase into ambient conditions.⁹ However, this β phase is metastable as it irreversibly transforms **back** into the α phase upon heating under ambient pressure.⁹

The atomic arrangement in these dimorphous forms are not similar and any $\alpha \rightarrow \beta$ transition would take place only after overcoming a high energy barrier (see Fig. 2(a,b)); only then Sr coordination changes from being at the center of a trigonal anti-prismatic cage into being at the center of square prismatic one; Al within the Al₂Si₂ slab changes from an AB-close-packed double-sheet into a planar square net; and the intralayer coordination of Si transforms from an umbrella-type into a square-pyramid one.

In this work, we show that all of the above empirical results (namely, HPHT synthesis routes,⁹ together with the structural and thermal events⁷⁻⁹) can be elegantly compiled into a single P - T diagram of transformations. Moreover, on the top of this empirical diagram, we superimpose another diagram composed out of the results obtained from room-temperature pressure-dependent synchrotron X-ray powder diffraction, XRPD, analysis and the pressure- and temperature-dependent free-energy calculations (in particular the prediction of reversible transitions and low-energy structural phases). The final construction is an equilibrium and nonequilibrium P - T diagram of transformations that highlights the character of the structural phases and the transformations (in particular the $P_c(T_c)$ boundaries that delineate the $\alpha \xrightarrow{P_c, T_c} \beta$ transitions).

It is expected that the inter-transformation among SrAl₂Si₂-dimorphs or complete chemi-

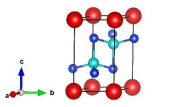
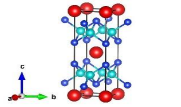
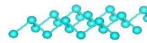

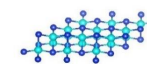
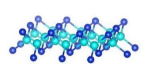


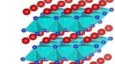
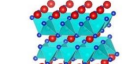
	α -SrAl ₂ Si ₂ P-3m1, experiment (T= 300 K, P= ambient)		β -SrAl ₂ Si ₂ I4/mmm, Ref.[9] (T=300 K, P= ambient)		
Unit Cell					
The bare Al layer					
AlSi ₂ slab					
Edge-sharing AlSi ₄ tetrahedrons					
3d atomic arrangement					
	This work (DFT)	Ref. [7]	This work (experiment)	This work (DFT, 0 GPa)	Ref. [9]
a [Å]	4.199	4.183	4.181	4.060	4.166
b [Å]	4.199	4.183	4.181	4.060	4.166
c [Å]	7.436	7.410	7.415	13.190	12.047
c/a	1.771	1.771	1.773	3.249	2.892
V [Å ³]	113.54	112.31	112.25	217.42	209.08
z	1	1	1	2	2
Density [g/cm ³]	2.90	2.92	2.92	3.02	3.14
α, β, γ	90, 90, 120	90, 90, 120	90, 90, 120	90, 90, 90	90, 90, 90
Sr	1a (0,0,0)	1a (0,0,0)	1a (0,0,0)	2a (0,0,0)	2a (0,0,0)
Al	2d (1/3,2/3,0.626)	2d (1/3,2/3,0.627)	2d (1/3,2/3,0.626)	4d (0,0.5,0.25)	4d (0,0.5,0.25)
Si	2d (1/3,2/3,0.276)	2d (1/3,2/3,0.276)	2d (1/3,2/3,0.265)	4e (0,0,0.385)	4e (0,0,0.374)

Figure 1: Comparison of the structural character of the α and β phases of SrAl₂Si₂. For α SrAl₂Si₂, the structure parameters were taken from Ref. 7, our experiments, and our optimized DFT-GGA analysis while the figures were adapted from Ref. 10 [Copyright (1988), with permission from Elsevier]. For β SrAl₂Si₂, the structure parameters were taken from Ref. 9 and our optimized DFT analysis while the figures were adapted from Ref. 7 [Copyright (2009), with permission from Elsevier] and Ref. 9 [Copyright (2017) American Chemical Society]. For both phases, the GGA calculations gave, as expected, weakly enlarged volumes as well as weakly softer bulk moduli (Table 2) than the experimental values.¹¹ Additionally, DFT calculations at P=5 GPa indicate $a=4.110$ Å and $c=7.210$ Å for α SrAl₂Si₂, while $a=4.102$ Å and $c=11.177$ Å for β SrAl₂Si₂. Bonding properties of each constituent ion were amply discussed in Refs.7,9. Symbols are as follows: Sr \equiv large-size red circle, Al \equiv intermediate-size cyan circle, Si \equiv small-size blue circle. All drawings of crystal structures were produced via VESTA program.¹²

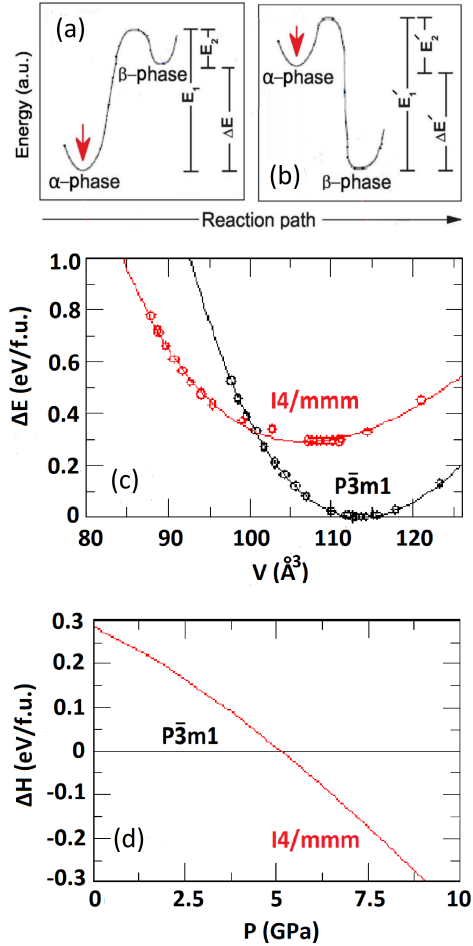


Figure 2: Free energies of SrAl₂Si₂ dimorphs. (a) Energy as a function of reaction path: α phase is at a global minimum (similar to the initial LPLT phase in Fig. 8). (b) β phase is at a global minimum while α phase is metastable (similar to the measured HPLT phase in Fig. 8, $P > P_c^{cal}$ and $k_B T < E_2'$). (c) Relative internal energy vs volume, $\Delta E(V)$, of SrAl₂Si₂. The solid lines are calculated from Murnaghan equation (Eq.1) for the two structural phases. (d) Relative enthalpy vs pressure, $\Delta H(P)$, curves with respect to the enthalpy of the most stable structure at zero pressure. The solid lines are calculated via Eq.3.

cal substitution within the α AAl₂Si₂ (A=Ca, Sr) isomorphs involves extensive atomic rearrangements or lattice parameters variation. This, in turn, is expected to have a direct impact on the related electronic structures. We are particularly interested in the evolution of the topology of the Fermi surfaces across the SrAl₂Si₂ dimorphs and α AAl₂Si₂ isomorphs as well as in how these modifications would be reflected in the (magneto-) transport properties. As an illustration, let us recall two features which are strikingly different among SrAl₂Si₂ dimorphs:⁷⁻⁹ the superconductivity (absent in α phase but emerging in β phase) and the sign of charge carriers (mixed in α phase while predominantly negative in β phase). As a further illustration, let us compare the electronic properties of the two α AAl₂Si₂ isomorphs: as that the evolution of transport properties of both compounds reflects contributions from hole and electron pockets,^{7-9,13} it is interesting to investigate whether the reported robust linear magnetoresistivity (LMR) of α CaAl₂Si₂¹³ is also manifested in isomorphous α SrAl₂Si₂. As far as the superconducting β SrAl₂Si₂ is concerned, this LMR feature is totally suppressed within the studied experimental conditions.⁹

This article is formatted as follows. In §2, we present the employed theoretical and experimental methods. In §3.1, we present zero-temperature and finite-temperature calculations. We show, in §3.2, our room-temperature pressure-dependent diffractograms and ambient-pressure temperature-dependent magnetoresistivity of α SrAl₂Si₂. We emphasize, in particular, that the experimental XRPD data do not evidence any $\alpha \rightarrow \beta$ transition up to 14 GPa, in contrast to the computational results; reconciliation of this discrepancy between prediction and experiment will be discussed in terms of nonequilibrium P - T diagram which is constructed in §3.2.3. Discussion and conclusion are given in §4.

2 Methods

2.1 Theoretical Techniques

Using the Quantum Espresso package,¹⁴ we initially performed full geometry optimizations for different target pressures ($P \leq 10$ GPa) and zero temperature. Our calculations are based on plane-wave basis sets and pseudopotentials. Ultra-soft Vanderbilt pseudopotentials,¹⁵ plane wave cutoff energy of 50 Ry and GGA-PBE exchange correlation functional¹⁶ were used. We considered 10, 3 and 4 valence-electrons pseudopotentials for Sr, Al, and Si, respectively.

The electronic band structure calculations were performed after geometry optimizations. The energy convergence criterion for the self-consistency loop was set to 10^{-7} eV and the lattice parameters and atomic positions were optimized until the forces on all atoms were smaller than 10^{-3} eV/Å. The electronic k-point mesh chosen was $10 \times 10 \times 10$.

The stability of the SrAl₂Si₂ dimorphs was verified by comparing the evaluated internal energy versus volume, $E(V)$, and enthalpy versus pressure, $\Delta H(P)$, of the most-probable structural candidates.¹⁷ All $E(V)$ curves are fitted to the Murnaghan equation-of-state:¹⁸

$$E(V) = B_0 V_0 \left[\frac{1}{B'_0(B'_0 - 1)} \left(\frac{V_0}{V} \right)^{B'_0 - 1} + \frac{V}{B'_0 V_0} - \frac{1}{B'_0 - 1} \right] \quad (1)$$

In Eq. 1, E is internal energy, V is volume, B_0 and B'_0 are the bulk modulus and its derivative with respect to pressure respectively; the subscript 0 denotes the zero-pressure values.

Following the procedures implemented in the Quantum Espresso code,¹⁹ we extracted elastic constants C_{ij} , after structure optimization, from the second derivative of the total energy with respect to the strain along two crystallographic directions:

$$C_{ij} = \frac{1}{V} \frac{\partial^2 E(V)}{\partial \varepsilon_i \partial \varepsilon_j}. \quad (2)$$

For hexagonal and tetragonal crystals, there are six independent elastic constants based on

Eq. 2: (C_{11} , C_{12} , C_{13} , C_{33} , C_{44} , C_{66}) and (C_{11} , C_{12} , C_{13} , C_{14} , C_{33} , C_{44}), respectively. We examined the pressure-dependence of these elastic constants (as well as the bulk moduli) at $P = 0$ and 5 GPa.

We also derived the pressure-dependent enthalpy, $H(P)$,:

$$H(P) = \frac{B_0 V_0}{B'_0 - 1} \left[\left(\frac{B'_0 P}{B_0} + 1 \right)^{1 - \frac{1}{B'_0}} - 1 \right], \quad (3)$$

and the $V(P)$ relation

$$V(P) = V_0 \left[1 + P \left(\frac{B'_0}{B_0} \right) \right]^{-1/B'_0}, \quad (4)$$

which is used in § 3.2.1 for comparing theory and experiment.

Finally, we performed DFT-based calculations of vibrational (phonon) spectra to compute vibrational contributions to the free energy of the SrAl₂Si₂ dimorphs, at various pressures. The quasi-harmonic approximation was used within the Quantum Espresso code.¹⁹ From these calculations, we extract the zero-point energy, entropy, and Gibbs free energy using standard expressions.²⁰ The free-energy analysis allows us to calculate the corresponding equilibrium P - T phase diagram.

2.2 Experimental Techniques

Sample preparation and experimental setups are the same as the ones described in Ref. 21. Polycrystalline samples were synthesized via standard Argon arc-melt procedure using high purity elements.

Diffraction patterns were collected *in situ* under high pressures exerted through a diamond anvil cell, at Xpress beamline - Elettra Sincrotrone Trieste, Italy²² - using a monochromatic beam of $\lambda = 0.4957$ Å. More details on the procedures adopted for high pressure diffraction measurements is described in Ref. 21.

Structural analyses were carried out using the Rietveld refinement as implemented in the Fullprof package.²³ During the refinement, the Wyckoff positions and site occupancy were

Table 1: Elastic constants (in [GPa]) and average Debye sound velocities of SrAl₂Si₂ dimorphs, under two representative pressures, as calculated via the DFT-GGA approximation. One verifies that the necessary and sufficient conditions for elastic stability for the two dimorphs, Eq. (5), are satisfied.

(GPa)	B ₀ [GPa]	B' ₀	v(m/s)	C ₁₁	C ₁₂	C ₁₃	C ₃₃	C ₁₄	C ₄₄	C ₆₆
<i>P</i> 3̄ <i>m</i> 1, 0 GPa	63.2	3.9	4538.76	141.7	26.5	26.4	129.9	0	40.3	-
<i>P</i> 3̄ <i>m</i> 1, 5 GPa	83.7	3.8	4889.07	177.1	40.0	39.0	163.9	0	52.9	-
<i>I</i> 4/ <i>mmm</i> , 0 GPa	62.0	4.4	3324.95	115.7	39.6	42.3	76.1	-	24.7	27.3
<i>I</i> 4/ <i>mmm</i> , 5 GPa	84.8	4.2	3777.31	132.5	73.0	63.0	111.6	-	46.9	59.2

Table 2: Experimental linear compressibilities ($\frac{\delta(a/a_0)}{\delta P}$, $\frac{\delta(c/c_0)}{\delta P}$) and bulk moduli and their derivatives (B₀ in [GPa] and B'₀), at T=300 K, of α SrAl₂Si₂. $\frac{\delta(a/a_0)}{\delta P}$ and $\frac{\delta(c/c_0)}{\delta P}$ (in TPa⁻¹) were obtained from a linear fit, close to P=0 GPa, of the data depicted in Figs. 6(a,b). All quantities are compared with the corresponding theoretical values obtained at P=0 GPa (See also Table 1). The strong correlation between B₀ and B'₀ parameters is depicted in the form of a confidence ellipse in Fig. 6(e). As the structure is more compressible along the *c*-axis, then the corresponding $|\frac{\delta(c/c_0)}{\delta P}|$ is higher than that along other axes [see text and Eqs. (6a,6b)]. Also shown are the predicted structural transformation and calculated critical pressure, P_c^{cal} in [GPa].

	$\frac{\delta(a/a_0)}{\delta P}$		$\frac{\delta(c/c_0)}{\delta P}$		B ₀		B' ₀		P_c^{cal}	α → β Transition
-	Exp.	Theor.	Exp.	Theor.	Exp.	Theor.	Exp.	Theor.		
Sr	-2.9(1)	-5.0	-4.1(1)	-5.6	64(9)	63.2	5(1)	3.9	5.0	<i>P</i> 3̄ <i>m</i> 1 → <i>I</i> 4/ <i>mmm</i>

fixed or varied depending on the conditions given in Space Group Tables. In particular, only the following parameters were allowed to vary: *z* of Al and Si in *P*3̄*m*1 and *z* of Si in *I*4/*mmm*. The sites preference and atomic displacement parameters were taken from the respective references quoted in Fig. 1.

Standard magnetization measurements were performed on a Vibrating Sample Magnetometer (VSM) while the electrical (magneto-)resistivity measurements on a standard four-probe dc-driven setup. Both were implemented in the Physical Property Measurement System (PPMS) of Quantum Design environment with a temperature range of 2 to 300 K and a magnetic field up to 90 kOe.

3 Results and Analysis

3.1 Theoretical Results

3.1.1 $T = 0$ K and $P \leq 10$ GPa calculations

Figures 2 (c, d) show the internal energy versus volume ($E(V)$ according to Eq. 1) and enthalpy versus pressure ($\Delta H(P)$ according to Eq. 3) for both the tetragonal *I*4/*mmm*²⁴ and the trigonal *P*3̄*m*1^{17,25} phases. In agreement with experiments, these figures indicate that, at ambient-

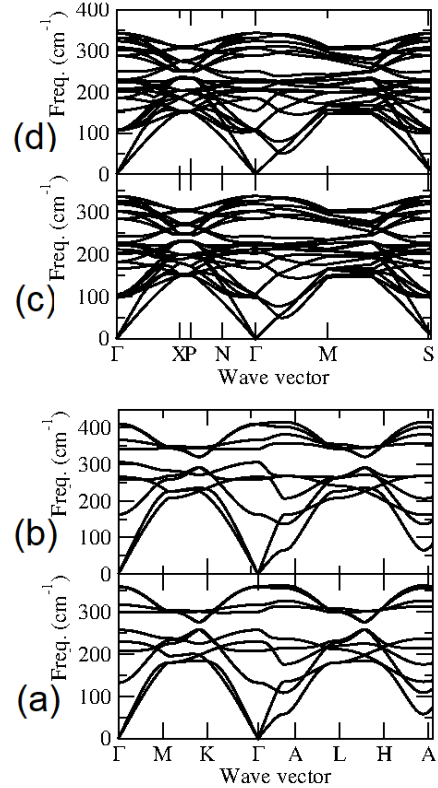


Figure 3: Vibrational dispersion curves of both α and β phases of SrAl₂Si₂ for two representative pressures: (a, b) α phase at P =0 GPa and P =8 GPa respectively. Similarly, (c, d) represent the corresponding curves of the β phase for both P =0 GPa and P =8 GPa, respectively.

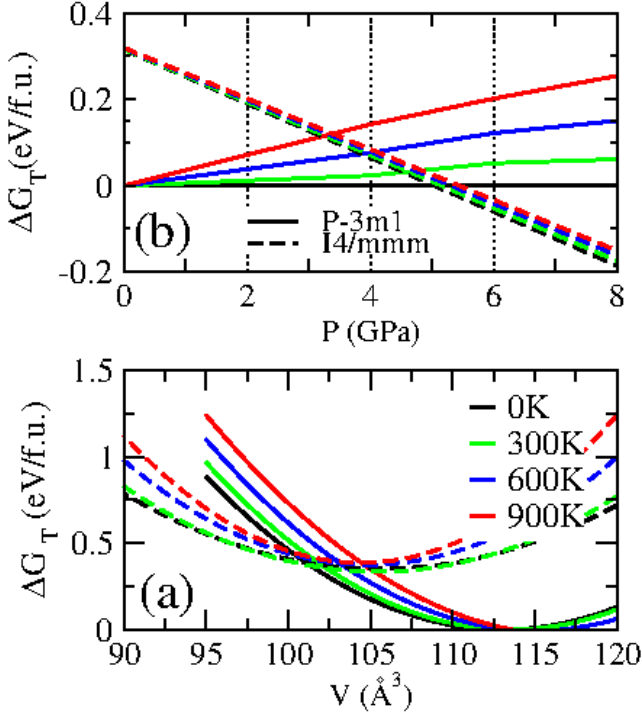


Figure 4: Evolution of Gibbs energies and the phase diagram of SrAl_2Si_2 . (a) Calculated isothermal Gibbs energy *versus* volume, $\Delta G_T(V)$, of α (solid lines) and β (dashed lines) phases. Similarly, (b) shows $\Delta G_T(P)$ of α (solid lines) and β (dashed lines) phases, using the same color code as in panel (a). Calculations were undertaken for $T = 0, 300, 600$ and 900 K. Energy reference was chosen to be that of α phase at zero-temperature. Based on the analysis of the curves in panel (b), one obtains the temperature-dependent critical pressure of $\alpha \xrightarrow{P_c(T_c)} \beta$ transition and therefrom constructs the P - T phase diagram shown in Fig. 8.

pressure, SrAl_2Si_2 crystallizes in the hexagonal $P\bar{3}m1$ phase. On the other hand, the $I4/mmm$ phase is the most stable one at sufficiently high pressures. In addition, on comparing the relative enthalpies of the studied phases, we are able to identify the critical pressure at which $\alpha \xrightarrow{P_c^{cal}} \beta$ transition occurs. The calculated $P_c^{cal} \approx 5.0$ GPa falls, as discussed in § 3.2.3, in the range of pressures employed during the *hot-compression cycle* to promote the $\alpha \xrightarrow{HPHT} \beta$ transformation ($4 < P \leq 9.5$ GPa and $400 \leq T \leq 1250$ °C,^{9,26}).

Table 1 summarizes the calculated bulk modulus, its derivative, and the elastic constants at selected pressures. Two points are worth mentioning: First, we verified that the mechanical stability criteria²⁷

$$\begin{aligned} C_{11} &> |C_{12}|, \quad C_{44} > 0, \\ 2C_{13}^2 &< C_{33}(C_{11} + C_{12}), \quad C_{66} > 0 \end{aligned} \quad (5)$$

are satisfied for both phases. Second, the observed pressure-induced increase in bulk modulus is indicative of an increased structural rigidity. But, as SrAl_2Si_2 is a layered structure, wherein the covalently-bond Al_2Si_2 slabs are stacked along the c -axis (Fig. 1), the baric evolution of their lattice parameters is expected to be anisotropic. Indeed, the calculated elastic constants indicate that $C_{11} > C_{33}$, i.e. compression along $[001]$ direction is easier than along $[100]$.

It is instructive to convert these elastic constants into linear compressibilities, since the latter are a useful measure of the anisotropy in the strength of intermolecular interactions.²⁸ Then, we are able to compare these theoretically-obtained compressibilities with the corresponding empirically-determined ones. For the hexagonal \vec{a} and \vec{c} directions, the following relations were employed:^{29,30}

$$\frac{\delta(a/a_o)}{\delta P} = -\frac{C_{33} - C_{13}}{C_{33}(C_{11} + C_{12}) - 2C_{13}^2} = -\beta_\alpha \quad (6a)$$

$$\frac{\delta(c/c_o)}{\delta P} = -\frac{C_{11} + C_{12} - 2C_{13}}{C_{33}(C_{11} + C_{12}) - 2C_{13}^2} = -\beta_c \quad (6b)$$

The converted compressibilities as well as the experimental ones are shown in Table 2 and will be discussed in § 3.2.1.

3.1.2 $0 < T \leq 900$ K and $P \leq 8$ GPa calculations

Representative vibrational dispersion curves, within $P \leq 8$ GPa, for α phase are shown in Figs.3(a, b) while that for β phase is in Fig.3(c, d). From the absence of imaginary frequencies in the Brillouin Zone, it is clear that both phases are dynamically stable within the studied pressure range. From the linear dispersion of the longitudinal acoustic modes, we calculate and show in Table 1 the average Debye sound velocities of the two dimorphs. As expected, the sound velocities are faster in the α phase because its bulk modulus (Table 1) is higher and its density (Fig. 1) is lower.

Figure 4(a) shows the calculated free energies at various fixed temperatures, ΔG_T vs V , while Fig. 4(b) shows the corresponding ΔG_T vs P curves. The latter ones allow us to obtain the temperature-dependent critical pressure of $\alpha \xrightarrow{P_c(T_c)} \beta$ transition and from there we construct the predicted P - T phase diagram shown in Fig. 8 (the thick blue solid line). Within this equilibrium analysis, the stable structure for $P < P_c(T_c)$ (blue hatched area) is the α phase whereas for $P > P_c(T_c)$ it is the β phase. We observe a monotonically increasing temperature-dependence of the critical pressure. The consequence of this distinct curve (as well as its distinct $\frac{dP}{dT}$) will be discussed in § 3.2.3.

3.2 Experimental Results

3.2.1 P -dependent structure of α SrAl_2Si_2 at 300 K

Representative pressure-dependent diffractograms of α SrAl_2Si_2 within the $P < 14$ GPa range are shown in Fig. 5. Measurements were conducted in two runs: the first up to 8 GPa while the second being performed so as to reach the 14 GPa range; both manifest a high degree of reproducibility within the

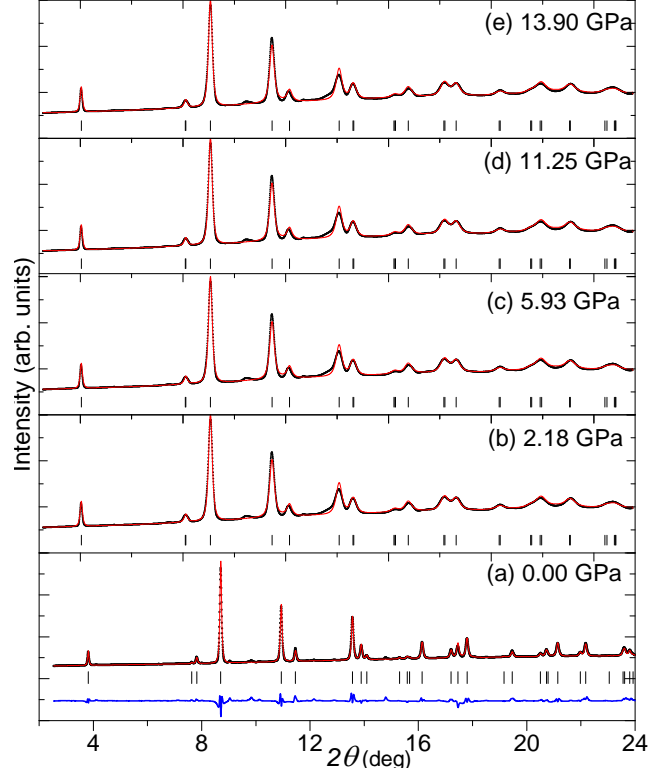


Figure 5: Selected pressure-dependent room-temperature diffractograms of α SrAl_2Si_2 for the following values: (a) ambient pressure, (b) 2.18 GPa, (c) 5.93 GPa, (d) 11.25 GPa, and (e) 13.90 GPa. *Symbols*: the measured intensities as symbols, Bragg positions as short vertical bars, and calculated intensities as continuous red lines. The difference between the measured and calculated intensities (as a blue line) is shown only in (a). As evident, the Bragg peaks at ambient pressure are sharper than those at higher pressures: Fig. S1 of the Supporting Information shows the baric evolution of both the full-width at half maximum and the area of (011)/(101) Bragg peak. Moreover, Table S1 shows the reliability factors χ^2 , R_p , R_{wp} for the studied diffractograms.

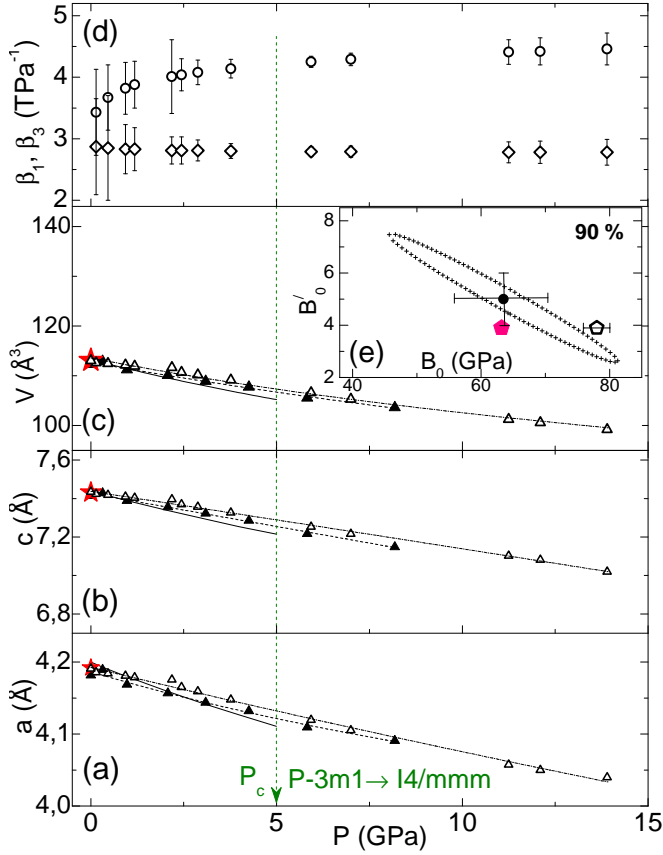


Figure 6: Baric evolution of room-temperature lattice parameters [a , c , V , respectively (a), (b) and (c)] of α SrAl_2Si_2 . *Symbols*: as obtained from the Rietveld analysis of Fig. 5. The lattice parameters of the two runs are shown as closed (first run) and open (second run) triangle symbols. *Red star symbol* represents the values after decompression. *Black solid line* represents the calculated lattice constants (no fitting, see text). *Thin dashed and dash-dot black lines* represent the fit parameters of the first and second runs, respectively, to Eq. 4 with the obtained B_0 and B'_0 as shown in Table 2. The vertical green arrow denotes P_c^{cal} . (d) Baric evolution of principal-axis compressibilities as obtained from the experimental data of panels (a,b) of second run; we used the online software PASCAL.³¹ The directions of the principal axes and their corresponding compressibilities with respect to the crystallographic axis are (0,0,1) for β_1 and (-0.942,0.334,0), (0.587,0.809,0) for β_2 , β_3 respectively. (*Inset (e)*) The 90% confidence ellipse,³² depicting the correlation between B_0 and B'_0 : being strongly elongated with a negative slope indicates that an increase in one leads to a reduction in the other and vice versa. Also drawn are the individual error bars for B_0 and B'_0 as obtained from their variance. *Pink closed pentagon symbol* represents the theoretical B_0 and B'_0 values of Table 1. *Black open pentagon symbol* represents the bulk modulus value $B_0=78(2)$ GPa after fitting with fixed $B'_0=3.9$.

common pressure range. Except for a very weak contamination with SrAlSi (less than 1 wt %), the Rietveld refinement of the diffractograms indicates a single $P\bar{3}m1$ phase with lattice parameters as given in Figs. 6(a-c) (see also Fig. 1). The diffractograms do not reveal any $P\bar{3}m1 \xrightarrow{HP,300K} I4/mmm$ transition, in apparent contradiction with theoretical prediction of §3.1. This contradiction is related to the presence of a separating high activation barrier which was not taken into consideration when assuming thermodynamic condition of equal free energies in §3.1. This same apparent discrepancy is evident in various other systems such as CaAl_2Si_2 ,²¹ and pressure-induced transformation (*diamond-cubic-phase* \rightarrow β -*Sn-phase*) in bulk Si.³³ In all cases, the absence of transformation within the experimental conditions is related to a large energy barrier that hinders any reconstructive paths that promote atomic and bonding rearrangements.³⁴

Figures 6(a-c) reveal a monotonically-decreasing lattice parameters, a behavior that confirms, satisfactorily, the theoretical predictions (solid lines) with no adjustable parameters within $P \leq P_c^{cal} \approx 5$ GPa range. In particular, when fitting the baric evolution of the measured volume to Eq.4, one obtains B_0 and B'_0 values shown in Table 2. The agreement between these empirically-determined B_0 and B'_0 and the theoretically-calculated ones (Table 2) is quite satisfactorily if one takes into consideration that the standard deviation of the fit are not small, that the fit is conducted within a restricted region that guarantees a satisfactory hydrostatic condition, and that there is a strong correlation among B_0 and B'_0 (as shown in the confidence ellipse³² in the Inset (e) of Fig. 6).

Finally, Table 1 compares the empirically-determined compressibilities $[\frac{\delta(a/a_0)}{\delta P}]$ and $\frac{\delta(c/c_0)}{\delta P}$ evaluated from Fig. 6(a,b)] with the theoretically-calculated compressibilities (see § 3.1.1 and Eqs. 6a, 6b). Evidently, these values do confirm the above-mentioned structural anisotropy which is related to the layered character: magnitudes of compressibilities along the c -axis are higher than those along the a -axis.

In addition, both theoretical and experimental values are very close to each other supporting the validity of our theoretical and empirical analyses.

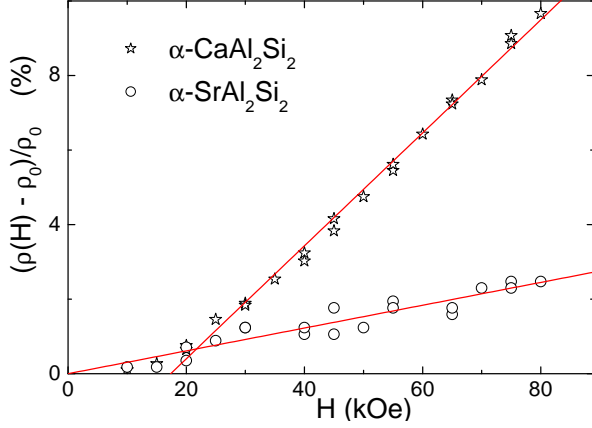


Figure 7: Magnetoresistivity of α SrAl₂Si₂ measured at 2.40(2) K and ambient-pressure. Comparison with the magnetoresistivity of α CaAl₂Si₂, measured at the same conditions, emphasizes its weak linear-in- H contribution (the linear slope of the Ca-based is 0.15%/kOe while that of Sr-based is 0.03%/kOe). That the fit of the magnetoresistivity of α CaAl₂Si₂ does not pass through the origin is due to the fact that the linear magnetoresistivity is only manifested above a certain threshold field.¹³

3.2.2 Isothermal Magnetoresistivity of α SrAl₂Si₂

We measured thermal evolution of both the magnetic susceptibility and electrical resistivity of α SrAl₂Si₂ and these do reproduce the corresponding curves reported in Refs. 7–9. As an illustration, the resistivity, shown in Fig. S2, does confirm the semimetallic character.⁹ As mentioned above, the diamagnetic susceptibility and the semimetallic resistivity as well as the reported negative sign of the Seebeck coefficient of α SrAl₂Si₂^{7,8} are consistent with the observation that the transport properties are dominated by the topology of the Fermi surfaces of hole and electron pockets.

On considering a rigid-energy-band approximation for both α AAl₂Si₂ (Fig. S3), one wonders whether the electrical properties (e.g. magnetoresistivity) of α SrAl₂Si₂ are similar to that of α CaAl₂Si₂.¹³ Fig. 7 shows

that the isothermal field-dependent normalized magnetoresistivity of α SrAl₂Si₂, measured at 2.4 K. Evidently, it is neither saturating nor quadratic-in- H ; rather, as compared to the reported linear-in- H magnetoresistivity of α CaAl₂Si₂, it exhibits a weak linear-in- H behavior, with the linear slope being almost 20 % of the value reported for its isomorph.¹³ This is attributed to the reduced contribution of the h_3 pocket which, according to Ref. 13, is the one which fulfills Abrikosov’s field and temperature conditions³⁵ required for the manifestation of linear magnetoresistivity.

3.2.3 Superposition of Empirical and Calculated P – T Diagrams

The calculated P – T diagram, delineated by the solid blue line in Fig. 8, is an equilibrium diagram which, as seen in §3.2.1, is in an apparent disagreement with experiment. As we mentioned above, the thermodynamic-equilibrium analysis of § 3.1 did not consider the activation barrier and as such this analysis is incapable of describing any nonequilibrium transformation or metastability. Accordingly, for constructing a diagram of transformations and for analyzing the synthesis and transformation routes, one should exercise particular care since different experimental P – T paths would not connect similar end-point polymorphic structural phases.^{2,3} We believe that the β phase is metastable and that its formation requires a much higher energy than that available at room temperature. Its formation requires the targeting of those P – T conditions whereat it is thermodynamically stable and afterwards follow the path wherein it can be kinetically trapped. Below we recall some synthesis procedures, involving different P – T trajectories, for the synthesis of the α and β phases: this allows the delineation of the phase boundaries.

The construction of the diagram of nonequilibrium transformations, Fig.8, is based on the following reported events (namely, the HPHT synthesis events and differential scanning calorimetry analysis):^{7,9,26} (i) Subjecting an initially room-temperature global-energy-minimum α phase to a HPHT treatment ($400 \leq$

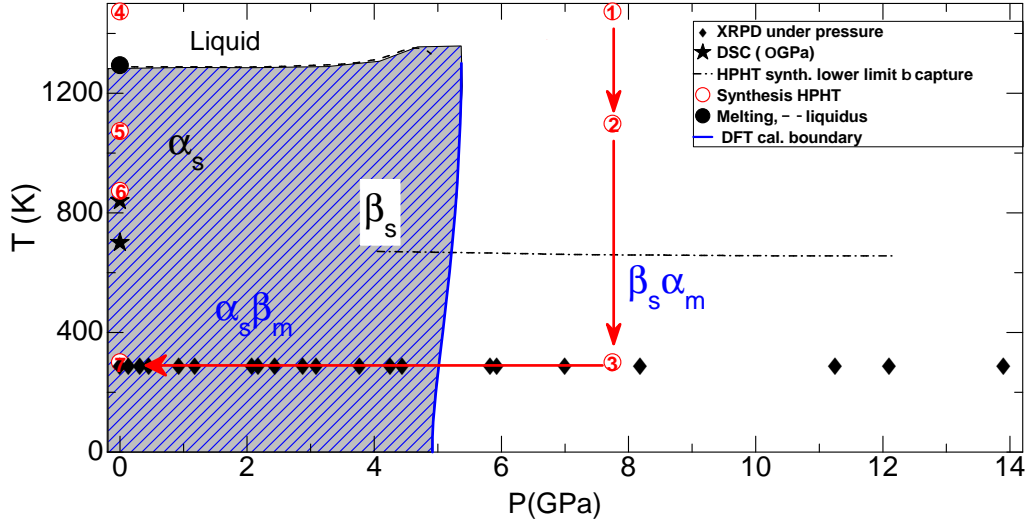
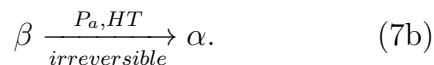
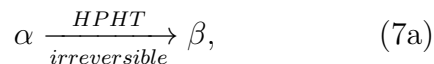


Figure 8: The equilibrium and nonequilibrium P - T diagram of SrAl_2Si_2 . The calculated equilibrium phase diagram, with boundaries marked by the blue line, is superimposed on the top of the diagram representing various experimental events as well as the extrapolated boundary lines. Information were collected from the synthesis data,^{9,26} the ambient-pressure thermal analysis,⁹ the ambient-pressure melting point,⁷ the XRPD analysis (Ref. 9, this work), and the DFT-based calculations (this work). As discussed in the text, the metastability region lies to the right of the blue hatched area. To identify and emphasize the meta/stable character, the corresponding phases are indicated as $\alpha_i\beta_j$ where $i,j \equiv s$ (stable) or m (metastable). The liquidus is represented by the upper, almost horizontal curve, while the dash-dot curve indicates the range above which the β phase can be quenched-and-captured; both curves are extrapolations that serve as visual guides. The long thick red arrows depict the path of the HPHT synthesis processes (1 \rightarrow 2 \rightarrow 3 \rightarrow 7). Ambient-pressure arc-melting/thermal treatment is indicated by the path 4 \rightarrow 5 \rightarrow 6 \rightarrow 7. Depending on the selected preparation route, some steps may be skipped. It is worth adding that a construction of a similar P - T diagram of CaAl_2Si_2 was hampered by its HPHT chemistry.^{21,36,37}

$T \leq 1250$ °C, $4 \leq P \leq 9.5$ GPa) followed by quenching under the same clamping pressure, the tetragonal β SrAl₂Si₂ is energetically trapped (the $7 \rightarrow 3 \rightarrow 1 \rightarrow 2 \rightarrow 3 \rightarrow 7$ route).

(ii) Subjecting an initially room-temperature-stabilized, metastable β phase to heating above 700 K under ambient-pressure and subsequent temperature ramp-down, the β phase is transformed, irreversibly, back into the α phase (the $7 \rightarrow 6 \rightarrow 7$ route).

These two observations can also be symbolically expressed as



The metastability character of SrAl₂Si₂, highlighted in Fig. 8, is a dominant feature within the studied P - T diagram: within the low-pressure blue-hatched region, the α phase is stable while the β phase is metastable (hence the label $\alpha_s\beta_m$). In contrast, within the high-pressure, white region, the stability is expected to be reversed (hence the label $\beta_s\alpha_m$).

The synthesis, the accessibility, the stabilization, and the functionality of each individual phase of SrAl₂Si₂ can be finely tuned by adjusting the control parameters (e.g. pressure, temperature, doping, and stoichiometry).³ In essence this amounts to a selection of a trajectory within the configuration space that leads to a specified local free-energy minimum (if one intends to trap a specific structure under ambient pressure and temperature, without being annealed into another structure).

The presence of the relatively high activation energy [separating e.g. the α and β phases, see Refs. 2,4,38 and Figs. 2(a, b)] marks a strong distinction among the various possible synthesis routes and, as a consequence, among the reversible/irreversible and equilibrium/nonequilibrium transformations, the different structural motifs and chemical bonding (Fig. 1), and different electronic structure (Fig. S3).

Considering the metastable polymorphism of SrAl₂Si₂, it is no surprise that there are various emergent functionalities of this compound: the

thermoelectricity,^{7,39} superconductivity,⁹ distinct thermal character (Seebeck, thermal conductivity,^{7,8} and specific heat⁹), quantum linear magnetoresistivity (this work), and, possibly topological Dirac semimetallicity.^{40,41}

It is worth mentioning that nonequilibrium transformation that traps a metastable phase (e.g. $\alpha \xrightarrow[\textit{P} \geq \textit{P}_c, \textit{T} \geq \textit{T}_c]{\textit{hot compression}} \beta$, Eq.(7a), afterwards rapid-quench under clamped-pressure) is a widely observed phenomenon.^{3,38,42} Generally such transformations lead to metastable structures: e.g. perovskite-related structures,⁴³ CaCO₃,⁴⁴ intermetallic disilicides/digerminides AX₂ (A= Ca, Sr, Ba; X=Si, Ge),⁴⁵⁻⁵⁰ rare-earth dantimonides RSb₂ (R=Dy - Lu,Y),⁵¹ HfO₂,³ V₂O₅,³ and AAl₂Si₂ (Sr, Ba).^{9,24,24,52}

4 Discussion and Conclusion

Generally, kinetic processes as those delineated in Fig.8 are influenced by various factors such as the energetics of the interfaces within the studied sample.⁵³ Accordingly, one expects that the phase boundaries in the diagram of Fig. 8 would depend on factors such as sample morphology and size, distribution of defects and strain, rate of heating, rate of applied pressure, and experimental time of observation. In fact, the exact value of e.g. the critical pressure of the $\alpha \rightarrow \beta$ transition is expected to be bound by a lower and an upper limit:³³ the lower bound is determined by the barrier-less thermodynamics analysis while the upper bound is manifested in defect- and strain-free cases wherein energy barrier is maximum. The observed values, due to the finite concentration of defects (acting as centres of phase nucleation) and accumulated strain in real samples, lie somewhere in between these two limits.^{33,53}

Finally, it is tempting, in spite of the irreversibility/metastability character, to employ the theoretical phase transformations of Fig. 8 so as to obtain a rough estimate of the latent heat L involved in the $\alpha \xrightarrow[\textit{P}_c, \textit{T}_c]{} \beta$ transition of SrAl₂Si₂. For that purpose, let us assume that

the Clausius–Clapeyron relation¹

$$L = T \Delta V \frac{dP}{dT}, \quad (8)$$

is valid across the calculated $P_c(T_c)$ phase boundary. Moreover, let us assume that L is similar to the one involved in the ambient-pressure high-temperature transition revealed in the DSC curves,⁹ Eq.(7b). Then, on substituting in Eq.(8) the experimental $T_c \approx 700$ K and theoretical $(\Delta V)_{T_c} \approx -0.035$ cm³/g and $(\frac{dP}{dT})_{T_c} \approx 0.44$ MPa/K, we obtain an exothermic $L_{cal} \approx -11$ J/g. It is assuring that the calculations do reproduce the correct sign (exothermic) of the reported transformation.⁹

In summary, our combined theoretical and experimental studies on pressure-dependent structural properties of SrAl₂Si₂ highlight its metastability and (non)equilibrium transformations. Our computational studies enabled the construction of the P – T phase diagram. However the ambient-temperature, high-pressure XRPD characterization does not follow the calculated equilibrium phase diagram. Based on the above analysis, we were able to reconcile the discrepancy between theory and experiment, to explain the stability/metastability of the α and β phases, to justify the requirement of HPHT treatment involving thermal shock to drive the transformation, and to follow the subsequent influence of the structural rearrangement on the topology of the Fermi surfaces and how this is manifested in the evolution of the electric transport properties.

As an outlook, let us recall that the diagram of Fig.8, being constructed out of limited number of structural, synthesis-routes, and thermal analyses, is preliminary and incomplete. Nevertheless, being a generalization and summary of all currently available experimental and theoretical information, it serves the purposes of identifying the (meta)stability regions and reconciling the discrepancy between our predictions and experiments. It is hoped that this diagram in particular and this work in general would motivate further theoretical and experimental investigations on, e.g, different P – T paths extended over expanded regimes

of HPHT experiments and detailed calculations of kinetic barriers. These further analyses would allow a better understanding of the correlation among the metastable structural motifs/trasformations, the electronic structure, the physico-chemical properties, and functionality of SrAl₂Si₂.

Supporting Information

Baric evolution of the normalized area and normalized Full-Width at Half Maximum of the most intense Bragg peak of α SrAl₂Si₂, zero-field and ambient-pressure resistivity, goodness of fit factors of Rietveld analysis of SrAl₂Si₂, and analysis of the electronic band structure and DOS of both α and β phases of SrAl₂Si₂ (a comparison with SrAl₂Si₂ CaAl₂Si₂ is also given).

Acknowledgments

We are grateful to CNPq, FAPERJ and FAPEMIG for partial financial support, to UFV computation cluster at Universidade Federal de Viçosa, to H. S. Amorim for useful discussion, and to Xpress beamline at Elettra Sincrotrone Trieste for allocating the beam time (Proposal 20185043). We are also grateful for partial support from project CALIPSOplus under Grant Agreement 730872 from the EU Framework Program for Research and Innovation HORIZON 2020.

A Supporting Information

Table S1: Reliability factors χ^2 , R_p , R_{wp} as obtained from Rietveld analysis of the diffractograms of α -SrAl₂Si₂ (see Fig.6 of the main text). These were obtained with no correction for background. More information on the chemical and structural parameters can be found in Figs. 1,6 of the main text.

P (GPa)	0	0.14	0.46	0.93	1.18	2.18	2.44	2.88	3.77	5.93	7.00	11.25	12.10	13.90
χ^2	1.41	2.58	2.59	3.02	3.21	3.46	3.14	4.14	4.43	3.74	3.64	3.51	3.85	4.35
R_p	1.44	1.58	1.60	1.83	1.92	2.03	2.06	2.14	2.27	2.06	2.04	1.98	2.04	2.20
R_{wp}	2.36	2.70	2.65	2.84	2.94	3.06	2.98	2.98	3.08	2.82	2.79	2.79	2.88	3.10

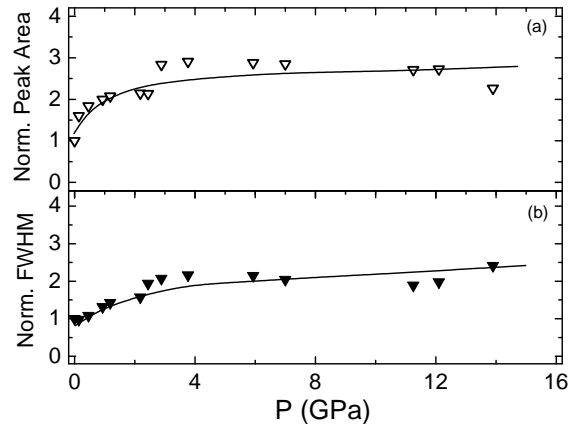


Figure S1: Baric evolution of (a) the normalized area and (b) normalized Full-Width at Half Maximum (FWHM) of the most intense Bragg, (011)/(101), peak of α -SrAl₂Si₂ (see Fig.6 of the main text). Black lines are guides to the eye.

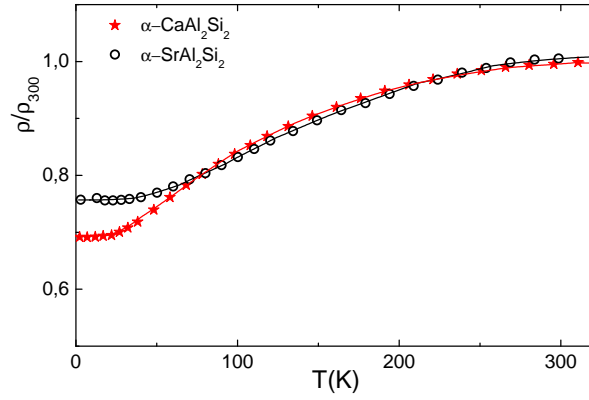


Figure S2: Thermal evolution of the normalized resistivity of α - SrAl_2Si_2 and α - CaAl_2Si_2 measured at ambient pressure and zero magnetic field. Both reveal characteristic semimetallic behavior,^{7,8} though that of α - SrAl_2Si_2 is relatively much weaker. A detailed discussion on the thermal evolution of the resistivity of these α - RAl_2Si_2 isomorphs can be found in Ref. 13. Black and red lines are guides to the eye.

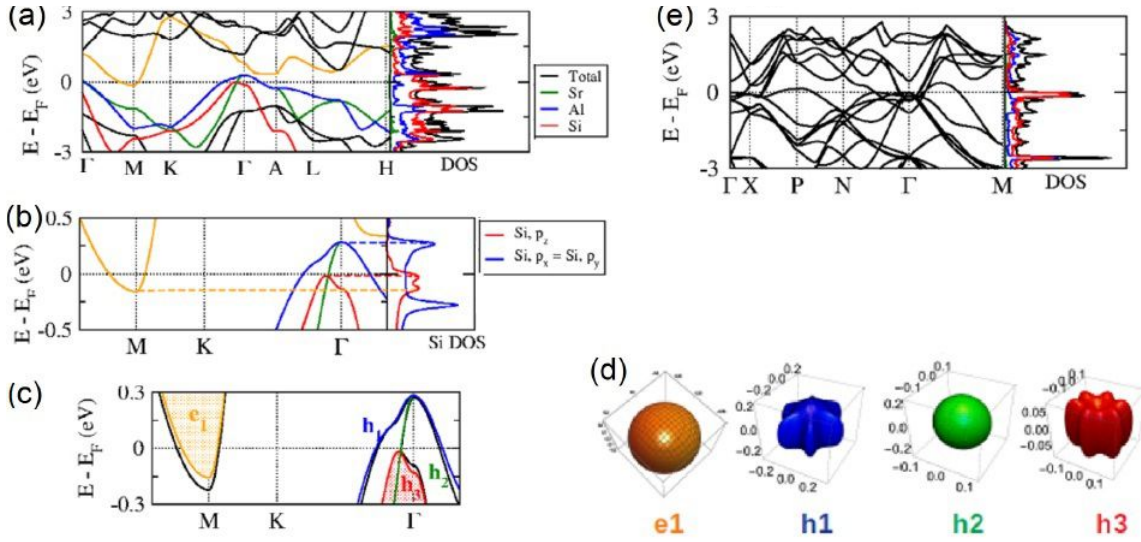


Figure S3: Electronic band structures of SrAl_2Si_2 . (a) Calculated electronic structure and total DOS of α - SrAl_2Si_2 . Near the Fermi level, the DOS is dominated by Si orbitals. (b) Expanded view of the electron pocket (e_1 , orange) and the three holes [h_1 (blue), h_2 (green), h_3 (red) pockets] along $\Gamma - K - M$ direction. The DOS is projected on the p atomic orbitals of Si. (c) Comparison of the bands structure of α - SrAl_2Si_2 (in color) and α - CaAl_2Si_2 (in black). (d) The Fermi surfaces of the contributing pockets: the larger-sized and almost spherical e_1 , h_1 , h_2 and (the almost 25% minor-in-height) h_3 . These are very similar to the corresponding Fermi surfaces of CaAl_2Si_2 .^{13,40} (e) Calculated electronic bands structure and total DOS of β - SrAl_2Si_2 . All structures were relaxed before the commencement of the electronic structure calculation.

B Electronic band structure and DOS analysis

DFT-based electronic band structure and total DOS of the α and β phases are shown in Figs. S3(a - d). These diagrams, in good agreement with Refs. 8,9, have direct relevance to the interpretation of the reported resistivity, Seebeck effect, thermal conductivity, thermoelectricity, and specific heat of these phases.⁷⁻⁹ The following three remarks illustrate such a relevance: (i) The increase in $N_t(E_F)$ of the β phase [Fig. S3(e)] is consistent with its superconducting properties.⁹ (ii) The configuration of multiple hole and electron pockets in the α phases is compatible with their semimetallicity being due to contributions from both the n-type and p-type carriers. (iii) This mixed contribution determines the strength of the magnetoresistivity as well as the sign and magnitude of both Hall and Seebeck effects.

For illustrating the last remark, let us compare the electronic structure of α SrAl₂Si₂ with that of isomorphous α CaAl₂Si₂. Figs. S3(b-c) exhibit, within the neighborhood of M and Γ points of both isomorphs, one electron pocket and three hole pockets; as evident, the total chemical substitution of Ca by the heavier and larger Sr (which amounts to a chemically-induced negative pressure) leads to some, though relatively weak, change in the configuration of hole and electron pockets of α SrAl₂Si₂. On the one hand, there is an upward shift of the conduction band minimum which is assumed to be due to an induced chemical pressure effect rather than to a purely, direct, chemical substitution: the partial density of states, pDOS, Figs. S3(a,b), indicates that, among the bands around the Fermi level, the major contributions is from Si orbitals rather than from Ca/Sr related ones.⁵⁷ There is also, on the other hand, a corresponding chemically-induced variation in the hole pockets (see Figs. S3(a,b)). As the free charge carriers in intrinsic compensated semimetal are expected to be equal, then a decrease (due to upwards shift relative to α CaAl₂Si₂) in the electron-pocket contribution would be accompanied by a decrease in the hole-pockets contribution. A better visualization can be gained if we consider the angular momentum projected density of states of Si atoms. This suggests that h_1 and h_2 hole pockets (both derived from p_x and p_y orbitals) are hardly influenced while both h_3 and e_1 pockets (both derived from p_z orbital) do exhibit a rearrangement, most dominantly anti-parallel shift. This reduced contribution of h_3 pocket, we argue in §3.2.2 of the main text, is the main reason behind the strong reduction in the linear-in- H magnetoresistivity of α SrAl₂Si₂.

Finally, it is recalled that the sign of the Seebeck coefficient of α SrAl₂Si₂ is negative within the whole measured temperature range.^{7,8} A similar Seebeck feature is evident in α CaAl₂Si₂.⁵⁸ Considering the above-mentioned compensated semimetallicity, the sign and magnitude of Seebeck coefficient must be related to the topology of the Fermi surface.⁵⁹ Fig. S3 shows the complexity of the Fermi surfaces of these pockets and, in addition, the large deviations from the simple parabolic band model. In spite of these complications, some insight can be gained if we adopt the following constant-relaxation-time approximation of the intrinsic bipolar Seebeck coefficient:^{59,60}

$$S = -\frac{k_B}{2q} \left[\frac{\sigma_e - \sigma_h}{\sigma_e + \sigma_h} \left(\frac{\epsilon_c - \epsilon_v}{k_B T} + 5 \right) + \frac{\epsilon_c + \epsilon_v - 2E_F}{k_B T} \right] \quad (\text{S9})$$

where k_B is Boltzmann constant, q is elementary charge, σ_e and σ_h are hole and electron conductivity, ϵ_c is the bottom of e_1 and ϵ_v is the top of the contributing h bands. Then, S of Eq.(S9) must be dictated by the conductivity ratio ($\frac{\sigma_e}{\sigma_h}$, depending on, e.g., the asymmetry of the effective masses) and the relative position of ϵ_c , ϵ_v and E_F . Figs. S3(b,c) show that the involved energy separations are very small, highlighting the decisive role of $\frac{\sigma_e}{\sigma_h}$. Accordingly, we consider this close proximity of ϵ_c , ϵ_v and E_F together with the major contribution of the e_1 pocket (leading to $\sigma_e > \sigma_h$) to be the main factors behind the negative sign and moderate magnitude of $S(T)$ of both α AAl₂Si₂ semimetals: for $A=\text{Sr}$, $-100 < S(T < 300 \text{ K}) < 0 \mu\text{V/K}$ ^{7,8} while for $A=\text{Ca}$,

$$-55 < S(T < 300 \text{ K}) < 0 \text{ } \mu\text{V/K.}^{58}$$

Synopsis: Using theoretical (free-energy, vibrational), empirical (X-ray powder diffraction), and reported (synthesis and thermal) analyses, we construct P - T phase diagram of transformations for SrAl_2Si_2 . There, semimetallic α SrAl_2Si_2 phase is separated from superconducting β SrAl_2Si_2 phase by a high activation barrier that can be surpassed only under high- P and high- T conditions. Indeed, although equilibrium free-energy calculation predict a $\alpha \xrightarrow{5\text{GPa}} \beta$ transition, room- T , P -dependent diffractogram show no structural transformation up to 14 GPa.

References

- (1) Blank, V. D.; Estrin, E. I. *Phase transitions in solids under high pressure*; CRC Press, 2013.
- (2) Brazhkin, V. V. Metastable phases, phase transformations, and phase diagrams in physics and chemistry. *Phys. Usp.* **2006**, *49*, 719.
- (3) Parija, A.; Waetzig, G. R.; Andrews, J. L.; Banerjee, S. Traversing energy landscapes away from equilibrium: strategies for accessing and utilizing metastable phase space. *J. Phys. Chem. C* **2018**, *122*, 25709.
- (4) Recio, J. M.; Menendez, J. M.; de la Roza, A. O. *An introduction to high-pressure science and technology*; CRC Press, 2015.
- (5) Bundy, F. Pressure-temperature phase diagram of elemental carbon. *Physica A: Statistical Mechanics and its Applications* **1989**, *156*, 169.
- (6) Angus, J. C.; Hayman, C. C. Low-pressure, metastable growth of diamond and "diamondlike" phases. *Science* **1988**, *241*, 913–921.
- (7) Kauzlarich, S. M.; Condrón, C. L.; Wassei, J. K.; Ikeda, T.; Snyder, G. J. Structure and high-temperature thermoelectric properties of SrAl_2Si_2 . *J Solid State Chem* **2009**, *182*, 240.
- (8) Lue, C.; Fang, C.; Abhyankar, A.; Lin, J.; Lee, H.; Chang, C.; Kuo, Y. Electronic structure and transport properties of SrAl_2Si_2 : Effect of yttrium substitution. *Intermetallics* **2011**, *19*, 1448.
- (9) Zevalkink, A.; Bobnar, M.; Schwarz, U.; Grin, Y. Making and Breaking Bonds in Superconducting $\text{SrAl}_{4-x}\text{Si}_x$ ($0 < x < 2$). *Chem. Mater.* **2017**, *29*, 1236.
- (10) Zheng, C.; Hoffmann, R. Complementary local and extended views of bonding in the ThCr_2Si_2 and CaAl_2Si_2 structures. *J. Solid State Chem.* **1988**, *72*, 58.
- (11) Narasimhan, S.; De Gironcoli, S. Ab initio calculation of the thermal properties of Cu: Performance of the LDA and GGA. *Physical Review B* **2002**, *65*, 064302.
- (12) Momma, K.; Izumi, F. *VESTA3* for three-dimensional visualization of crystal, volumetric and morphology data. *J. Appl. Crystallogr.* **2011**, *44*, 1272.
- (13) Costa, D. G.; Capaz, R. B.; Falconi, R.; Strikos, S.; ElMassalami, M. Linear magnetoresistivity in layered semimetallic CaAl_2Si_2 . *Sci Rep* **2018**, *8*, 4102–4112.
- (14) Giannozzi, P., et al. QUANTUM ESPRESSO: a modular and open-source software project for quantum simulations of materials. *J. Phys.: Cond. Mat.* **2009**, *21*, 395502–395521.

- (15) Vanderbilt, D. Soft self-consistent pseudopotentials in a generalized eigenvalue formalism. *Phys. Rev. B* **1990**, *41*, 7892–7895.
- (16) Perdew, J. P.; Burke, K.; Ernzerhof, M. Generalized Gradient Approximation Made Simple. *Phys. Rev. Lett.* **1996**, *77*, 3865–3868.
- (17) In fact we carried out the comparative analysis for the following four possible phases:²¹ orthorhombic *Pnma*,^{54,55} orthorhombic *Cmcm*,^{24,56} tetragonal *I4/mmm*,²⁴ and trigonal *P $\bar{3}$ m1*²⁵ phases. For brevity we limit our description to only the two low-lying phases which were observed experimentally.
- (18) Murnaghan, F. D. Finite deformations of an elastic solid. *Amer. J. Math.* **1937**, *59*, 235–260.
- (19) Baroni, S.; Giannozzi, P.; Isaev, E. Density-Functional Perturbation Theory for Quasi-Harmonic Calculations. *Rev. Mineral Geochem.* **2010**, *71*, 39.
- (20) Baroni, S.; Giannozzi, P.; Isaev, E. Thermal properties of materials from ab-initio quasi-harmonic phonons. *Rev. Mineral Geochem.* **2011**, *71*.
- (21) Strikos, S.; Joseph, B.; Alabarse, F. G.; Valadares, G.; Costa, D. G.; Capaz, R. B.; ElMas-salami, M. Pressure dependence of room-temperature structural properties of CaAl₂Si₂. *J. Phys.: Condens. Matter* **2020**, *32*, 365403.
- (22) Lotti, P.; Milani, S.; Merlini, M.; Joseph, B.; Alabarse, F.; Lausi, A. Single-crystal diffraction at the high-pressure Indo–Italian beamline Xpress at Elettra, Trieste. *J. Synchrotron Radiat.* **2020**, *27*, 222.
- (23) Rodriguez-Carvajal, J. Recent Developments of the Program Fullprof. *IUCr CPD Newsletter* **2001**, *26*, 12.
- (24) Yamanaka, S.; Kajiyama, M.; Sivakumar, S. N.; Fukuoka, H. Preparation and Single-Crystal Structure of a New High-Pressure Modification of BaAl₂Si₂. *High Pressure Res.* **2004**, *24*, 481.
- (25) Gladyshevskii, E.; Kripyakevich, P.; Bodak, O. Crystal structure of SrAl₂Si₂ and its analogs. *Ukr. Phys. J* **1967**, *12*, 447–452.
- (26) Zevalkink, A. On the high-temperature and high-pressure synthesis of SrAl₂Si₂. 2020; Private communication.
- (27) Mouhat, F.; Coudert, F.-X. Necessary and sufficient elastic stability conditions in various crystal systems. *Phys. Rev. B* **2014**, *90*, 224104.
- (28) Stevens, L. L.; Eckhardt, C. J. The elastic constants and related properties of β -HMX determined by Brillouin scattering. *The Journal of chemical physics* **2005**, *122*, 174701.
- (29) Nye, J. F., et al. *Physical properties of crystals: their representation by tensors and matrices*; Oxford university press, 1985.
- (30) Kimizuka, H.; Ogata, S.; Li, J.; Shibutani, Y. Complete set of elastic constants of α -quartz at high pressure: a first-principles study. *Phys. Rev. B* **2007**, *75*, 054109.
- (31) Cliffe, M. J.; Goodwin, A. L. PASCAL: a principal axis strain calculator for thermal expansion and compressibility determination. *Journal of Applied Crystallography* **2012**, *45*, 1321.

- (32) Gonzalez-Platas, J.; Alvaro, M.; Nestola, F.; Angel, R. EosFit7-GUI: a new graphical user interface for equation of state calculations, analyses and teaching. *J. Appl. Crystallogr.* **2016**, *49*, 1377.
- (33) Mizushima, K.; Yip, S.; Kaxiras, E. Ideal crystal stability and pressure-induced phase transition in silicon. *Phys. Rev. B* **1994**, *50*, 14952.
- (34) Sharma, S. M.; Sikka, S. Pressure induced amorphization of materials. *Prog. Mater. Sci.* **1996**, *40*, 1.
- (35) Abrikosov, A. Quantum magnetoresistance of layered semimetals. *Phys. Rev. B* **1999**, *60*, 4231.
- (36) Tanaka, M.; Zhang, S.; Inumaru, K.; Yamanaka, S. High-Pressure Synthesis and Superconductivity of the Laves Phase Compound $\text{Ca}(\text{Al},\text{Si})_2$ Composed of Truncated Tetrahedral Cages $\text{Ca}@\text{(Al, Si)}_{12}$. *Inorg. Chem.* **2013**, *52*, 6039.
- (37) Tanaka, M.; Zhang, S.; Tanaka, Y.; Inumaru, K.; Yamanaka, S. High pressure synthesis and crystal structure of a ternary superconductor $\text{Ca}_2\text{Al}_3\text{Si}_4$ containing layer structured calcium sub-network isomorphous with black phosphorus. *J. Solid State Chem.* **2013**, *198*, 445.
- (38) Turnbull, D. Metastable Structures in Metallurgy. *Metall Trans* **1981**, *12B*, 217.
- (39) Zevalkink, A.; Zeier, W. G.; Cheng, E.; Snyder, J.; Fleurial, J.-P.; Bux, S. Nonstoichiometry in the Zintl phase $\text{Yb}_{1-\delta}\text{Zn}_2\text{Sb}_2$ as a route to thermoelectric optimization. *Chem. Mat.* **2014**, *26*, 5710.
- (40) Su, H.; Shi, X.; Xia, W.; Wang, H.; Hanli, X.; Yu, Z.; Wang, X.; Zou, Z.; Yu, N.; Zhao, W., et al. Magnetotransport and ab initio calculation studies on the layered semimetal CaAl_2Si_2 hosting multiple nontrivial topological states. *Phys. Rev. B* **2020**, *101*, 205138.
- (41) Deng, T.; Chen, C.; Su, H.; He, J.; Liang, A.; Cui, S.; Yang, H.; Wang, C.; Huang, K.; Jozwiak, C., et al. Electronic structure of the Si-containing topological Dirac semimetal CaAl_2Si_2 . *Phys. Rev. B* **2020**, *102*, 045106.
- (42) Ponyatovsky, E.; Barkalov, O. Pressure—induced amorphous phases. *Mater. Sci. Rep.* **1992**, *8*, 147.
- (43) Hagenmuller, P., Ed. *Preparative Methods in Solid State Chemistry*; Academic Press, 1972.
- (44) Bayarjargal, L.; Fruhner, C.-J.; Schrodtt, N.; Winkler, B. CaCO_3 phase diagram studied with Raman spectroscopy at pressures up to 50 GPa and high temperatures and DFT modeling. *Phys. Earth Planet. Inter.* **2018**, *281*, 31.
- (45) Evers, J.; Oehlinger, G.; Weiss, A. Effect of pressure on the structures of divalent metal disilicides MSi_2 (M= Ca, Eu, Sr). *J. Solid State Chem.* **1977**, *20*, 173.
- (46) Evers, J. Transformation of three-connected silicon in BaSi_2 . *J. Solid State Chem.* **1980**, *32*, 77.
- (47) Imai, M.; Hirano, T.; Kikegawa, T.; Shimomura, O. Phase transitions of BaSi_2 at high pressures and high temperatures. *Phys. Rev. B* **1998**, *58*, 11922.
- (48) Imai, M.; Kikegawa, T. Phase transitions of alkaline-earth-metal disilicides $\text{M}_{\text{AE}}\text{Si}_2$ (M_{AE} = Ca, Sr, and Ba) at high pressures and high temperatures. *Chem. Mater* **2003**, *15*, 2543.

- (49) Wang, J.-T.; Chen, C.; Kawazoe, Y. Phase stability and transition of BaSi₂-type disilicides and digermanides. *Phys. Rev. B* **2015**, *91*, 054107.
- (50) Nishii, T.; Mizuno, T.; Mori, Y.; Takarabe, K.; Imai, M.; Kohara, S. X-ray diffraction study of amorphous phase of BaSi₂ under high pressure. *Phys. Status Solidi B* **2007**, *244*, 270.
- (51) Merrill, L. Behavior of the AB₂-Type Compounds at High Pressures and High Temperatures. *J. Phys. Chem. Ref. Data* **1982**, *11*, 1005.
- (52) Narita, Y.; Kume, T.; Sasaki, S.; Shimizu, H.; Maekawa, S.; Kikudome, T.; Yamanaka, S. High-pressure Raman study of nano-channel materials: BaAl₂Si₂ and BaSi₆. *J. Phys. Conf. Ser.* **2008**, *121*, 162002.
- (53) Chen, C.-C.; Herhold, A. B.; Johnson, C. S.; Alivisatos, A. P. Size dependence of structural metastability in semiconductor nanocrystals. *Science* **1997**, *276*, 398.
- (54) Condrón, C. L.; Hope, H.; Piccoli, P. M. B.; Schultz, A. J.; Kauzlarich, S. M. Synthesis, Structure, and Properties of BaAl₂Si₂. *Inorg. Chem.* **2007**, *46*, 4523.
- (55) Nolas, G. S. *The physics and chemistry of inorganic clathrates*; Springer, 2014; Vol. 199.
- (56) Carrillo-Cabrera, W.; Paschen, S.; Grin, Y. EuGa_{2±x}Ge_{4±x}: preparation, crystal chemistry and properties. *J. Alloys Compd.* **2002**, *333*, 4.
- (57) Peng, W.; Chanakian, S.; Zevalkink, A. Crystal chemistry and thermoelectric transport of layered AM₂X₂ compounds. *Inorg. Chem. Front.* **2018**, *5*, 1744.
- (58) Kuo, Y.-K.; Sivakumar, K.; Tasi, J.; Lue, C. S.; Huang, J.; Wang, S.; Varshney, D.; Kaurav, N.; Singh, R. The effect of Al/Si ratio on the transport properties of the layered intermetallic compound CaAl₂Si₂. *Journal of Physics: Condensed Matter* **2007**, *19*, 176206.
- (59) Markov, M.; Rezaei, S. E.; Sadeghi, S. N.; Esfarjani, K.; Zebarjadi, M. Thermoelectric properties of semimetals. *Phys. Rev. Materials* **2019**, *3*, 095401.
- (60) Mahan, G. D. Good Thermoelectrics. *Solid State Phys.* **1988**, *51*, 81.

Graphical TOC Entry

